Article:
Li, X., Liu, H., Du, H. et al. (6 more authors) (2023) Carbon defect induced evolution of structural and mechanical properties in substoichiometric (HfMoNbZr)Cx films. Tribology International, 190. 109034. ISSN 0301-679X

https://doi.org/10.1016/j.triboint.2023.109034

Carbon defect induced evolution of structural and mechanical properties in substoichiometric (HfMoNbZr)C_x films

Xiaoyang Li[a], Hao Liu[a], Hao Du[a,b*], Fugui Zhang[a], Jie Shi[c], Hengning Hu[c], Mingqiang Xie[c], Liuquan Yang[d], Houfu Dai[e*]

[a] *School of Mechanical Engineering, Guizhou University, Guiyang 550025, PR China*

[b] *State Key Laboratory of Public Big Data, Guizhou University, Guiyang 550025, PR China*

[c] *Chengdu Tool Research Institute CO., Ltd., Chengdu 610500, PR China*

[d] *School of Mechanical Engineering, University of Leeds, Leeds LS2 9JT, United Kingdom*

[e] *Department of Mechanical Engineering, Shantou University, Shantou 515063, PR China*

* Corresponding authors.

E-mail address: hdu3@gzu.edu.cn (H. Du), houfudai@stu.edu.cn (H. Dai)

Postal address: School of Mechanical Engineering, Guizhou University, Guiyang, 550025, PR China

Abstract

Substoichiometric (HfMoNbZr)C_x films with varied carbon content were synthesized using non-reactive magnetron sputtering. Findings reveal that the (HfMoNbZr)C_x film predominantly exhibits a single-phase FCC structure, which transforms to a dual-phase structure consisting of FCC and Hex. phases at higher carbon content. This behavior arises from the segregation of group VB (Nb) and VIB (Mo) elements from the FCC lattice. The film hardness (*H*) and elastic modulus (*E*) increases with rising carbon content accompanied by a decrease of coefficient of friction (COF). However, the wear rate is not decreased despite the increased *H* and reduced COF of the as-deposited films. This phenomenon is explained by examining the differences in the wear mechanisms between (HfMoNbZr)C_x films with single- and dual- phase structures.

Keywords: multi-principal element carbides, dual-phase structure, hardness, tribological behavior

1 Introduction

The carbide films exhibit high hardness [1], exceptional wear resistance [2], excellent corrosion resistance [3], and remarkable radiation stability [4], making them widely employed as protective coatings for applications in aerospace, nuclear reactors, cutting tools, and biomedical fields. In recent years trends is to improve film properties further by alloying multiple elements. Particularly, the introduction of the innovative concept of material design, namely high-entropy alloys (HEAs), has significantly sparked research interest in multi-principal element carbides (MPECs) as film materials with enhanced performance [5–8]. The concept of MPECs is derived from HEAs, wherein the material comprises five or more metallic elements with nearly equal atomic ratios [9]. The exceptional properties obtained beyond those of individual constituents are believed to stem from thermodynamic high-entropy effects, crystallographic lattice distortion effects, and kinetic hysteresis diffusion effects [10–12]. Furthermore, the incorporation of carbon into the multi-principal element system is proposed to enhance hardness without compromising ductility, thereby offering greater possibilities for MPECs [13,14]. For instance, investigations on (CrNbTaTiW)C films have demonstrated that the incorporation of carbon atoms, attributed to their smaller atomic size, induces significant lattice distortion, resulting in a more pronounced additional hardening effect than conventional solid solution strengthening mechanisms, thereby resulting in a substantial augmentation in film hardness [15]. Likewise, the hardness enhancement has been observed in (CrNbSiTiZr)C films [16]. Additionally, the incorporation of carbon atoms elicits a grain refinement phenomenon and an improve in film density, thereby fostering enhancement in film hardness, which has been proved in other studies [17,18]. Consequently, the manipulation of carbon defect concentrations allows for tailoring the mechanical properties of MPECs.

The constituent cations also significantly affect the mechanical properties of MPECs. Strong carbide-forming cations in groups IVB, VB, and VIB, such as Hf, Nb, and Zr, readily form Me-C bonds with strong covalent characteristics, thereby increasing the thermodynamic stability and hardness of MPECs [19]. With a big difference, weak carbide forming elements, such as Fe, Co, Ni, decreases the solubility of carbon in the crystals, and lead to complex crystal structures and the formation of precipitates and amorphous carbon matrix in the film [20,21]. For instance, the (Mo-Ta-W)-C and (Nb-Ta-W)-C films demonstrate exceptional hardness and elastic modulus, achieving remarkable values of 35.5 and 36.1 GPa, and 343.3 and 349.5 GPa, respectively [22]. Similarly, (TiZrNbHfTa)C film exhibits high hardness of 31 GPa and outstanding wear resistance with a low coefficient of friction (COF) of approximately 0.12 [23]. In comparison, the

(CoCrFeMnNi)C film possesses maximum hardness and elastic modulus values of 16 GPa and 183 GPa, respectively [21].

Aiming to obtain high hardness of films as protective hard coatings for tribological applications, we select refractory elements from group IVB to VIB as cations, where, Hf, Nb, and Zr are strong carbide-forming elements, while Mo is a medium-strong carbide-forming element with great potential for reducing the COF in high-temperature tribological environments [24]. (HfMoNbZr)C_x films with varying carbon defect concentrations were prepared using non-reactive direct current magnetron sputtering (dcMS). We investigated the elemental composition, cross-sectional morphologies, bonding characteristics, as well as the mechanical and tribological properties of (HfMoNbZr)C_x films.

2 Experimental details

(HfMoNbZr)C_x films were deposited using 3-inch $Hf_{25}Mo_{25}Nb_{25}Zr_{25}$ (99.95% purity) and graphite (99.98% purity) targets in a high vacuum deposition system with a base pressure of 2×10^{-3} Pa. Single-side polished 10 × 10 mm sized silicon (001) and 20 × 20 mm sized sapphire (0001) wafers were used as substrates (sapphire substrates were only used for tribology test). Si and sapphire wafers were ultrasonically cleaned by petroleum ether and ethanol, respectively, and blown dry by air before being mounted on the substrate holder. The substrate was placed opposite to the targets at a distance of 11 cm with an angle of 45° between substrate plane and the surface of targets. Prior to the deposition, the substrates were heated at a temperature of 500 °C and maintained for 10 min to ensure that the substrate holder was thoroughly heated. No etch cleaning was carried out for the substrates. The deposition was carried out at a working pressure of 4.5×10^{-1} Pa, where Ar was introduced into the chamber at a gas flow rate of 40 sccm. During the deposition, $Hf_{25}Mo_{25}Nb_{25}Zr_{25}$ and graphite targets were powered by dcMS power supplies. The discharge power for the $Hf_{25}Mo_{25}Nb_{25}Zr_{25}$ target was kept at 150 W, while the graphite target power (P_C) was set to 0, 45, 60, 80, 100, and 120 W, respectively, by regulating the discharge current. The substrate potential was kept floating during the deposition. The deposition time for each section were kept at 180 min. Samples were taken out of the chamber as the temperature of the substrate holder was cooled down to 80 °C.

The cross-sectional morphologies of (HfMoNbZr)C_x films were examined by a Scanning Electron Microscope (SEM, Gemini 300, Zeiss) with an accelerating voltage of 3.0 kV. The elemental composition of as-deposited films was determined by Electron Probe Microanalyses (EPMA, JEOL JAX8230) with the aid of the ZAF-corrected program and an accelerating voltage of 15 kV. The X-ray diffractometer (XRD,

D8 Advance, Bruker) with Cu Kα radiation wavelength of 0.154056 nm was applied to investigate the crystallographic structures of the films in a Bragg-Brentano geometry. The recorded 2θ range was 20 - 80° with a scanning speed of 2° per min. X-ray photoelectron spectroscopy (XPS) measurements were performed in the Thermo Scientific K-Alpha system with employing Al Kα (hv=1486.6 eV) as the X-ray source. Prior to the spectrum collection, the samples were sputter-etched for 30 nm using Ar^+ ion beam the contaminations on to remove the surface contaminations. The sputter etching was performed under a base pressure of 2×10^{-5} Pa, with the application of charge neutralization. During this process, the incident angle of Ar^+ was set at 58°, and it possessed an energy level of 2000 eV. The high-resolution spectra were carried out in pass energy of 50 eV and step size of 0.1 eV. For each spectrum, the binding energy scale was calibrated by examining the raw valence band spectra around Fermi energy to avoid problems caused by the use of C 1s [25].

The hardness (*H*) and elastic modulus (*E*) of the (HfMoNbZr)C_x films were measured by a nanoindenter (TTX-NHT2, Anton Paar) equipped with a Berkovich tip. The measurement was carried out in the load of 10 mN, and *H* and *E* were obtained from the load-displacement curve following the Oliver and Pharr method [26]. In order to ensure the accuracy of the measurements, 10 indentations were conducted for each specimen at varied locations of the film surface area and the maximum depth less than 1/10 of the films thickness was maintained. The tribological performance of (HfMoNbZr)C_x films were studied using the films grown on sapphire substrate by a ball-on-disc tribometer (MFT-4000, Huahui) at room temperature. The sliding was in a linear reciprocating mode with a Φ 6 mm Al_2O_3 ball as the counterpart. The sliding speed, load, and time was set as 200 mm·min^{-1}, 5 N, and 100 min, respectively. The area of the 5 mm-long wear tracks was examined by the three-dimensional 3D Optical Profilometer (Contour Elite K, Bruker). The wear rates (W_r) of films were calculated using the equation [27]:

$$W_r = \frac{V}{F \cdot S}$$

Where *V* represents the wear volume (m^3), *F* is the normal load (N), and *S* is the total sliding distance (m).

The special quasi-random structures (SQSs) were generated using the mcsqs code [28] of the Alloy-Theoretic Automated Toolkit (ATAT) [29]. $(Hf_{0.25}Mo_{0.25}Nb_{0.25}Zr_{0.25})C$ solid solution, i.e., a 2 × 2 × 2 SQS supercell with 64 atoms in cubic B1 (FCC) structure, was constructed. The density of states of the film was calculated by ab-initio calculations based on density functional theory (DFT) [30]. The first-principles calculations were performed using the Vienna Ab Initio Simulation Package (VASP) [31]. The projection

augmented wave (PAW) [32] method was used to simulate the interaction between ions and electrons. The generalized gradient approximation (GGA) with the Perdew-Burke-Ernzerhof (PBE) potential as proposed by Perdew et al. [33,34] was used to describe the exchange correlation function. Brillouin zone sampling was performed using 1 × 1 × 1 Γ-centered scheme. The energy convergence of self-consistency cycles and ionic relaxation was set up as EDIFFG = 1E-6 and EDIFF = 1E-4, respectively. The energy volume curve was fitted by using the third-order Birch-Murnaghan equation of state (EOS) [35]. The pre- and post-processing of calculation results are carried out by VESTA [36] and VASPKIT [37] software.

3 Results

3.1 Composition and crystal structure

Elemental compositions and the atomic ratio between carbon and the total metallic elements (*C/Me*) of (HfMoNbZr)C_x films deposited at varied P_C are shown in Fig. 1. As seen in Fig. 1 (a), the element concentration of metallic atoms in the film is nearly equiatomic. With increasing P_C, the carbon concentration also increases, reaching a maximum value of 33.8% at P_C = 120 W, where the *C/Me* reaches the value of ~ 51% (see Fig. 1 (b)).

X-ray diffractograms, out-of-plane lattice constant a_0, and full width at half maximum FWHM of the (HfMoNbZr)C_x films are shown in Fig. 2. As can be seen in Fig. 2 (a), the HfMoNbZr alloy film exhibits a fine BCC crystallographic structure, characterized by a single broad peak with (110) preferred orientation located at 2θ = 36.4°. Upon increasing the P_C from 45 W to 120 W, a transition in the crystallographic structure of the as-deposited films is observed, with the emergence of FCC structure accompanied by preferential orientations of (111), (200), (220), and (222). The position of 111 peak shifts to lower 2θ angles with the increasing P_C accompanied by an increase of peak intensity. In addition, for the films grown at P_C values of 80 W, 100 W, and 120 W, additional reflections corresponding to the hexagonal-structured MeC_x phase are identified, characterized by (004) and (100) preferred orientations at 2θ = 30.8° and 32.8°, respectively. As seen in Fig. 2 (b), the out-of-plane lattice constant (a_0) of (HfMoNbZr)C_x gradually increases with the increase of P_C, consistent with the shift observed in the 111 peak. In contrast, the FWHM of the (HfMoNbZr)C_x films gradually decreases, indicating an increase of crystallite size of (111) plane composed crystallites in the out-of-plane direction.

The cross-sectional morphology of (HfMoNbZr)C_x films deposited at different P_C are shown in Fig. 3. The HfMoNbZr alloy film (P_C = 0 W) exhibits a clearly defined fine-grained structure, consistent with

observations reported elsewhere [38]. With the introduction of carbon element, the growth of the film changes toward columnar structure. However, no significant variation in the film growth rate is observed across different P_C values.

The chemical bonds of the (HfMoNbZr)C_x films with different P_C are determined using XPS spectra. Fig. 4 shows high-resolution XPS spectra recorded over the C 1s, Hf 4f, Mo 3d, Nb 3d, and Zr 3d core-level regions for the (HfMoNbZr)C_x films with a sputter-etching depth of 30 nm. As shown in Fig. 4 (a), the C 1s peaks located at around 282.57 eV and 284.83 eV correspond to metal carbides and C-C hybrids, respectively [39]. The intensity of the binding energy corresponding to the metal carbide increases with the increase of the P_C, while the intensity and location of C-C hybrids remain unchanged. This increase in carbide content is accompanied by shifts in the Hf 4f [40,41], Mo 3d [42–44], Nb 3d [45–47], and Zr 3d [48,49] spectra, as shown in Fig. 4 (b)-(e), indicating a transition from metallic bonds to Me-C bonds with the increase of P_C. Notably, the Mo 3d and Nb 3d spectra peaks shift to the binding energy of Mo_2C [43] and Nb_2C [46] at P_C = 60 W and to higher binding energies corresponding to MoC [44] and NbC [47] at P_C = 120 W. This shift is significantly different from that observed in other constituting metallic elements, namely Hf 4f and Zr 3d. This phenomenon suggests the presence of novel Mo-C and Nb-C bonds at higher P_C, which aligns with the dual-phase feature observed in the x-ray diffractograms (Fig, 3) [50–52]. In Fig. 4 (f), the intensity of the O 1s spectrum is weakened at higher P_C, indicating a lower fraction of the metal-oxygen bond. This phenomenon is confirmed in both the Hf 4f (Fig. 4 (b)) and Zr 3d (Fig. 4 (e)) spectra, where the intensity of the Hf-O bond (17.48 eV) [53] and Zr-O bond (at 182.97 eV) [54] decreases with increasing P_C. Overall, these XPS results provide further evidence supporting the XRD results, demonstrating that the formation of carbides is enhanced with the increasing carbon defect concentration in film crystals.

3.2 Mechanical property and tribological performance

The hardness (H), elastic modulus (E), H/E, and H^3/E^{*2} of (HfMoNbZr)C_x films grown at different P_C are shown in Fig. 5. For the film grown at P_C = 0 W, the H and E are 13.2 ± 0.3 GPa and 155.4 ± 1.9 GPa, respectively. As P_C increases, the film H and E significantly increases and reaches maximum value of 31.7 ± 0.7 GPa and 297.1 ± 8.4 GPa, respectively, at P_C = 120 W (Fig. 5 (a)). As seen in Fig. 5 (b), the H/E and H^3/E^{*2} of the (HfMoNbZr)C_x films increase with the increase of P_C, where higher H/E and H^3/E^{*2} represent higher elastic strain to failure and enhanced resistance of the film to plastic deformation [55,56].

Fig. 6 depicts the COF curve and the average COF of (HfMoNbZr)C_x films under ball-on-disk test. As seen in Fig. 6 (a), the COF curves of the (HfMoNbZr)C_x films increase rapidly during the transition period, and then reach to a relatively steady-state period. For the film grown at P_C = 0 W, the COF initially reached a value of ~ 0.75 which produces a significant fluctuation at approximately 5 min, followed by a steady-state period with the COF value of ~ 0.4 until the end of test. It can be compared with the films grown at P_C in the range of 45 W – 120 W, where no significant fluctuation of COF in the transition period is seen. Such a high drop of COF for P_C = 0 W case is expected to be resulted from the fully wear-out of HfMoNbZr alloy film after the significant fluctuation as its *H* is relatively low as compared with (HfMoNbZr)C_x. This can be also identified by the wear track depth and wear rate of P_C = 0 W film (Fig. 6 (c) and (d)) that the local depth of wear track exceeds the film thickness (Fig. 3(a)). As a result, the low average COF obtained by HfMoNbZr alloy film is mainly from that between Al_2O_3 counterpart and sapphire substrate (see Fig. 6 (b) and Fig. S2). With the increase of the P_C, the average COF of (HfMoNbZr)C_x films decreases, and the minimum value is obtained by the film grown at P_C of 120 W (Fig. 6 (b)). The 2D profiles of wear tracks and wear rate of the (HfMoNbZr)C_x films are shown in Fig. 6 (c) and (d). As seen in Fig. 6 (c), the depth and the width of the wear track of the HfMoNbZr alloy film is far greater than the (HfMoNbZr)C_x films. With the P_C increases from 45 W to 120 W, the depth of the wear tracks of the (HfMoNbZr)C_x films slightly increase, where the depth reaches the maximum value at P_C of 120 W. This phenomenon is highly correlated with the estimated wear rate of as-deposited films. As seen in Fig. 6 (d), the HfMoNbZr alloy film possesses the highest wear rate. For (HfMoNbZr)C_x films, it is clear that even though the film *H* increases and COF decreases simultaneously with the increase of P_C, the wear rate still increases as P_C increases from 45 W to 80 W, followed by nearly equal wear rate of the films grown at P_C of 80, 100, and 120 W. This phenomenon is in consistent with the wear behavior of tungsten carbide films shown in Ref. [57]. However, main difference between the P_C = 80, 100, and 120 W cases is that wear tracks of the (HfMoNbZr)C_x becomes smoother with the increasing P_C.

3.3 Electronic structure

In order to further study the bonding characteristics of the (HfMoNbZr)C_x film, the density of states (DOS) of the stoichiometric ($Hf_{0.25}Mo_{0.25}Nb_{0.25}Zr_{0.25}$)C is calculated. The theoretical calculation results of the total density of states (TDOS) and partial density of states (PDOS) of the constituting elements are shown in Fig. 7. The ($Hf_{0.25}Mo_{0.25}Nb_{0.25}Zr_{0.25}$)C exhibits an obvious bonding-antibonding structure with a pseudogap feature, which has been reported in the study of early carbides [58,59]. As shown in Fig. 7 (a), the Fermi

level is located near the minimum value of TDOS, indicating the structural stability of $(Hf_{0.25}Mo_{0.25}Nb_{0.25}Zr_{0.25})C$. The observed total density of states curve can be divided into three regions: (i) The first region, ranges from -13.3 eV to -8.7 eV, is mainly dominated by C *p* states. (ii) The second region, located at -7.3 eV to 0.2 eV, is mainly dominated by Me *d* states (Me = Hf, Mo, Nb and Zr) and C *p* states of the metal. (iii) The third region is ranged from 0.2 eV to 3.5 eV and located above the Fermi level, where the main contribution is from the *d* states of Mo and Nb, and the contribution of C *p* state is small. In addition, in the second region the C *p* and Me *d* states have a significant resonance, which indicates strong covalent properties [60]. The hybridization between Me *d* electrons and C *p* electrons is supposed to rationalize the high hardness of carbides [61].

4. Discussion

4.1 Bonding and crystallographic structure

For all the $(HfMoNbZr)C_x$ films, the carbon content increases with increasing P_C. However, the value of *C/Me* reaches only around 51% at P_C = 120 W, which is still lower than 1:1, indicating substoichiometry of the films. Despite the low carbon content, crystalline FCC-structured Me-C phases are still observed in the x-ray diffractograms (Fig. 2(a)). This can be attributed to the predominant formation of carbides by consuming the metallic atoms rather than amorphous carbon, resulting in crystalline carbides with carbon vacancies in the film. The preferential formation of carbides is further supported by the analysis of Raman spectroscopy data (see Fig. S3), which did not show any significant signals from C-C sp^2 or C-C sp^3 bonds. Although weak peaks of C-C sp^2 and C-C sp^3 bonds are observed in the C 1s core-level spectrum (Fig. 4(a)), no noticeable changes are observed as P_C increases from 60 W to 120W. As P_C increases, the crystallinity of the carbides improves (see Fig. 2(a)), accompanied by the growth of the film from a fine-grained structure towards a columnar structure (see Fig. 2(c) and Fig. 3). This phenomenon is commonly observed in sputter-deposited substoichiometric carbide films, where crystallinity increases with increasing carbon content [62]. In addition, it is seen in Fig. 2 the higher P_C leads to an increase in the lattice parameter (a_0) of carbide grains. It can be attributed to the higher insertion number of carbon atoms at interstitial positions within the B1-structured lattice [63].

We are particularly interested in drawing conclusions regarding the appearance of the hexagonal-structured MeC_x phase when $P_C \geq 80$ W (see Fig. 2 (a)). According to the phase diagram of binary carbides, Mo and Nb have a tendency to form a crystal structure with hexagonal Me_2C and MeC coexisting at low

carbon content, while Hf and Zr can only form the B1-structured MeC [64]. The hexagonal-structured Me_2C can diffuse into the B1-type solid solution with HfC or ZrC as the host materials [65–69]. Consequently, a single-phase FCC crystallographic structure can be identified in the film grown at P_C of 45 W and 60 W (Fig. 2 (a)). However, due to the higher number of valence electrons in elements from group VB (Nb) and VIB (Mo), the stability of this solid solution is low, and it decreases further as carbon vacancies decrease, i.e., when more carbon defects are introduced [70]. As a result, the increasing carbon content in the film inevitably leads to the formation of a secondary hexagonal MeC_x phase [71]. The tendency of Mo and Nb to segregate from the solid solution is also supported by the mixing enthalpies of binary Me-C systems, where the mixing enthalpies of Hf-C, Mo-C, Nb-C, and Zr-C are −123, −67, −102, and −131 KJ/mol, respectively [72], indicating the lower stability of Mo-C and Nb-C systems compared to Hf-C and Zr-C systems. Additionally, the formation of the secondary hexagonal phase by Mo and Nb is consistent with the peak shifts observed in the XPS spectra (Fig. 4), where the atomic chemical bond states of Mo 3d and Nb 3d shift from metallic to Me_2C and MeC at P_C of 60 W and 120 W, respectively. As carbon atoms receive electrons from metallic atoms, the increase of P_C results in higher binding energy values [73,74]. This shift to the left, i.e., a higher binding energy value, is observed in the XPS spectrum at higher P_C is also suggested elsewhere [75,76]. In summary, the presence of a dual-phase crystallographic structure at $P_C \geq 80$ W is primarily attributed to the complex nature of Mo-C and Nb-C phases at varied carbon contents.

4.2 Mechanical and tribological properties

In this study, the H of the obtained multi-principal carbide film is higher than that of other related studies [15,17]. Additionally, the H and E of the (HfMoNbZr)C_x film are significantly elevated with the addition of carbon, as comparing the P_C of 0 W and 45 W cases. This enhancement can be attributed to the formation of carbides that exhibit a mixture of covalent-metallic-ionic chemical bonding in (HfMoNbZr)C_x (see Fig. 7) [77]. As the P_C is further increased, the volume of crystallite carbides increases, leading to a higher H [78]. Moreover, when P_C is increased from 80 W to 120 W, a dual-phase structure emerges, as confirmed by XRD analysis (Fig. 2 (a)). Similar to high-entropy alloys, the presence of a dual-phase structure is supposed to significantly increase H and E of the film, owing to distinct plastic deformation mechanisms and interface interactions within the dual-phase structure [79–81]. It is also suggested that the incorporation of the secondary phase stabilizes the FCC matrix, resulting in improved mechanical properties of the film [82,83]. Additionally, as discussed in the Section 4.1, both XPS (Fig. 4) and Raman spectra (Fig. S3) demonstrate no significant increase in the formation of C-C sp^2 or C-C sp^3 bonds with increasing P_C,

providing an explanation for the observed increase in film hardness as the presence of an amorphous carbon matrix would cause mechanical deterioration of the film.

The film coefficient of friction (COF) decreases with the increase of P_C, as shown in Fig. 6 (a) and (b). As discussed previously, the formation of C-C sp^2 or C-C sp^3 bond is not significantly enhanced with the increasing P_C. Therefore, we believe the decrease of COF when comparing P_C = 0 W, 45 W, 60 W cases is due to the segregation of carbon during sliding against the Al_2O_3 counterpart [1,84]. During the reciprocating friction process, heat generation prompts the graphite crystals in the film's grain boundary to precipitate onto the surface. These graphite crystals subsequently interact with atmospheric water and oxygen, creating a friction transfer layer that serves as a lubricant during wear [49]. Evidence of this can be found in the Raman spectra of the wear scar, where distinct D and G peaks are observable in P_C = 45 W films (see Fig. S3 (b)), contrasting with the absence of apparent C-C peaks in the as-deposited film. However, the reason of further decline in COF for dual-phase structured (HfMoNbZr)C_x films (P_C = 80 W, 100 W, and 120 W) may differ, as no conspicuous D and G peaks are seen in the wear scar (see Fig. S3). This reduction in COF could be attributable to the lubricative quality of the hexagonal-structured MXenes [85].

Regarding the wear rate of (HfMoNbZr)C_x films grown at varied P_C, shown in Fig. 6 (c) and (d), at a P_C of 45 W, the wear track depth curve of the film exhibits a "W-shaped" profile. This pattern is ascribed to the plastic deformation of wear debris at the film-counterpart interface during wear (see Fig. S4 (a) and (a_1)) [57], and as a result reveals a wear scar exhibiting adhesive wear morphology. In contrast, the film grown at P_C = 120 W presents a smoother appearance without noticeable deformation of wear debris (Fig. S4 (b) and (b_1)). Further investigation of the morphology and elemental composition of wear debris for P_C = 45 W and 120 W films (Fig. S5 and Table S1) reveals a greater abrasive size for the P_C = 120 W film, partially accounting for its higher wear rate [86]. Furthermore, the increased oxygen content in the wear debris of the P_C = 45 W film indicates more extensive oxidation during the tribology process. Thus, we speculate that the mechanism explaining the elevated wear rate of the P_C = 120 W film compared to the P_C = 45 W film stems from variations in wear mechanism and debris morphology.

5 Conclusions

In this study, we demonstrate that the film structure and properties of (HfMoNbZr)C_x films are highly dependent on variations in the point defect density of carbon. We find that (HfMoNbZr)C_x films containing

less than 25.4 at. % carbon display a single-phase NaCl-type FCC structure, while those with higher carbon content induce a dual-phase composition of FCC and hexagonal phases. Interestingly, no conspicuous C-C bonding formation is found in the film even when the P_C reaches 120 W, achieving a *C/Me* ratio of approximately 51%, as validated by both X-ray photoelectron spectroscopy and Raman spectra. Our evidence points to the second phase's emergence stemming from the low stability of Nb-C and Mo-C compared to other constituent carbide bonds. Furthermore, both hardness and elastic modulus are correlated with increasing carbon content, peaking at 31.7 ± 0.7 GPa and 297.1 ± 8.4 GPa, respectively, at a P_C of 120 W. Elevating the carbon content also effectively diminishes the coefficient of friction (COF) of the films, reaching a COF of 0.4 at P_C = 120 W. However, the minimal wear rate of 3.8×10^{-15} $m^3/(N\cdot m)$ is achieved by the film grown at P_C = 45 W, accompanied by a COF and hardness of 0.64 and 20.8 ± 0.6 GPa, respectively. We speculate that the reduced wear rate of (HfMoNbZr)C_x films grown at P_C = 45 W, compared to those at P_C = 120 W, is related to differences in wear mechanisms and debris morphology. This research furnishes fresh insights into the effects of carbon content on the structure and attributes of (HfMoNbZr)C_x films, uncovering new opportunities to tailor the properties of multi-element carbide (MEPC) films through anion defect manipulation.

Acknowledgments

The work is financially supported by the National Natural Science Foundation of China (Grant No. 52165021, 51805102, 52105178, and 12162008), Guizhou Provincial Science and Technology Innovation Center (Grant No. [2023]010), and the Guizhou University Cultivation Project (Grant No. [2019] No. 25). H. Du is grateful for the financial support from SINOMACH (Grant No. JG04KF0202301) and the backing of the State Key Laboratory of Public Big Data, Guizhou University. Dr. Jianjun Hu at University of South Carolina is appreciated for the help and support for DFT calculations.

CRediT author statement

Xiaoyang Li: Conceptualization, Investigation, Data curation, Formal analysis, Writing – original draft. **Hao Liu:** Data curation, Writing – review & editing. **Hao Du:** Project administration, Conceptualization, Supervision, Writing – review & editing, Funding acquisition. **Fugui Zhang:** Investigation, Writing – review & editing, Funding acquisition. **Jie Shi:** Investigation, Data curation, Formal analysis, Writing – review & editing. **Hengning Hu**: Investigation, Writing – review & editing. **Mingqiang Xie**: Investigation, Writing – review & editing. **Liuquan Yang**: Conceptualization, Investigation, Writing – review & editing.

Houfu Dai: Project administration, Conceptualization, Supervision, Writing – review & editing, Funding acquisition.

Data availability

The data that support these findings are available from the corresponding author on request.

Competing interests

The authors declare no competing interests.

References

[1] J. Hu, H. Li, J. Li, J. Huang, J. Kong, H. Zhu, D. Xiong, Structure, mechanical and tribological properties of TaCx composite films with different graphite powers, Journal of Alloys and Compounds. 832 (2020) 153769. https://doi.org/10.1016/j.jallcom.2020.153769.

[2] M. Braic, V. Braic, M. Balaceanu, C.N. Zoita, A. Vladescu, E. Grigore, Characteristics of (TiAlCrNbY)C films deposited by reactive magnetron sputtering, Surface and Coatings Technology. 204 (2010) 2010–2014. https://doi.org/10.1016/j.surfcoat.2009.10.049.

[3] W. Yan, Y. Zhang, L. Chen, J. Luo, P. Pang, X. Zhang, B. Liao, M. Ying, Corrosion behavior and interfacial conductivity of amorphous hydrogenated carbon and titanium carbide composite (a-C: H/TiC) films prepared on titanium bipolar plates in PEMFCs, Diamond and Related Materials. 120 (2021) 108628. https://doi.org/10.1016/j.diamond.2021.108628.

[4] M.A. Tunes, S. Fritze, B. Osinger, P. Willenshofer, A.M. Alvarado, E. Martinez, A.S. Menon, P. Ström, G. Greaves, E. Lewin, U. Jansson, S. Pogatscher, T.A. Saleh, V.M. Vishnyakov, O. El-Atwani, From high-entropy alloys to high-entropy ceramics: The radiation-resistant highly concentrated refractory carbide (CrNbTaTiW)C, Acta Materialia. 250 (2023) 118856. https://doi.org/10.1016/j.actamat.2023.118856.

[5] H. Ju, M. Athmani, J. Luan, A. AL-Rjoub, A. Cavaleiro, T.B. Yaqub, A. Chala, F. Ferreira, F. Fernandes, Insights into the oxidation resistance mechanism and tribological behaviors of multilayered TiSiN/CrVxN hard coatings, Int. J. Miner. Metall. Mater. (2023). https://doi.org/10.1007/s12613-023-2655-0.

[6] H. Du, R. Shu, R. Boyd, A.L. Febvrier, M.A. Sortica, D. Primetzhofer, U. Helmersson, P. Eklund, D. Lundin, Corundum-structured AlCrNbTi oxide film grown using high-energy early-arriving ion irradiation in high-power impulse magnetron sputtering, Scripta Materialia. 234 (2023) 115578. https://doi.org/10.1016/j.scriptamat.2023.115578.

[7] Q. Sun, H. Tan, S. Zhu, Z. Zhu, L. Wang, J. Cheng, J. Yang, Single-phase (Hf-Mo-Nb-Ta-Ti)C high-entropy ceramic: A potential high temperature anti-wear material, Tribology International. 157 (2021) 106883. https://doi.org/10.1016/j.triboint.2021.106883.

[8] H. Ju, K. Huang, J. Luan, Y. Geng, J. Yang, J. Xu, Evaluation under temperature cycling of the tribological properties of Ag-SiNx films for green tribological applications, Ceramics International. 49 (2023) 30115–30124. https://doi.org/10.1016/j.ceramint.2023.06.267.

[9] R. Shu, H. Du, G. Sadowski, M.M. Dorri, J. Rosen, M.A. Sortica, D. Primetzhofer, D. Lundin, A. Le Febvrier, P. Eklund, Multicomponent TixNbCrAl nitride films deposited by dc and high-power impulse magnetron sputtering, Surface and Coatings Technology. 426 (2021) 127743. https://doi.org/10.1016/j.surfcoat.2021.127743.

[10] U. Jansson, E. Lewin, Carbon-containing multi-component thin films, Thin Solid Films. 688 (2019) 137411. https://doi.org/10.1016/j.tsf.2019.137411.

[11] M. Braic, M. Balaceanu, A. Vladescu, C.N. Zoita, V. Braic, Deposition and characterization of multi-principal-element (CuSiTiYZr)C coatings, Applied Surface Science. 284 (2013) 671–678. https://doi.org/10.1016/j.apsusc.2013.07.152.

[12] H. Du, R. Shu, R. Boyd, A. Le Febvrier, U. Helmersson, P. Eklund, D. Lundin, Evolution of microstructure and properties of TiNbCrAlHfN films grown by unipolar and bipolar high-power impulse magnetron co-sputtering: The role of growth temperature and ion bombardment, Surface and Coatings Technology. 459 (2023) 129389. https://doi.org/10.1016/j.surfcoat.2023.129389.

[13] Z. Wang, I. Baker, Interstitial strengthening of a f.c.c. FeNiMnAlCr high entropy alloy, Materials Letters. 180 (2016) 153–156. https://doi.org/10.1016/j.matlet.2016.05.122.

[14] Z. Wang, I. Baker, W. Guo, J.D. Poplawsky, The effect of carbon on the microstructures, mechanical properties, and deformation mechanisms of thermo-mechanically treated Fe40.4Ni11.3Mn34.8Al7.5Cr6 high entropy alloys, Acta Materialia. 126 (2017) 346–360. https://doi.org/10.1016/j.actamat.2016.12.074.

[15] P. Malinovskis, S. Fritze, L. Riekehr, L. von Fieandt, J. Cedervall, D. Rehnlund, L. Nyholm, E. Lewin, U. Jansson, Synthesis and characterization of multicomponent (CrNbTaTiW)C films for increased hardness and corrosion resistance, Materials & Design. 149 (2018) 51–62. https://doi.org/10.1016/j.matdes.2018.03.068.

[16] Y.-S. Jhong, C.-W. Huang, S.-J. Lin, Effects of CH4 flow ratio on the structure and properties of reactively sputtered (CrNbSiTiZr)Cx coatings, Materials Chemistry and Physics. 210 (2018) 348–352. https://doi.org/10.1016/j.matchemphys.2017.08.002.

[17] B. Osinger, H. Mao, S. Fritze, L. Riekehr, U. Jansson, E. Lewin, Investigation of the phase formation in magnetron sputtered hard multicomponent (HfNbTiVZr)C coatings, Materials & Design. 221 (2022) 111002. https://doi.org/10.1016/j.matdes.2022.111002.

[18] V. Braic, A. Vladescu, M. Balaceanu, C.R. Luculescu, M. Braic, Nanostructured multi-element (TiZrNbHfTa)N and (TiZrNbHfTa)C hard coatings, Surface and Coatings Technology. 211 (2012) 117–121. https://doi.org/10.1016/j.surfcoat.2011.09.033.

[19] E. Lewin, K. Buchholt, J. Lu, L. Hultman, A.L. Spetz, U. Jansson, Carbide and nanocomposite thin films in the Ti–Pt–C system, Thin Solid Films. 518 (2010) 5104–5109. https://doi.org/10.1016/j.tsf.2010.03.017.

[20] J. Chen, Z. Yao, X. Wang, Y. Lu, X. Wang, Y. Liu, X. Fan, Effect of C content on microstructure and tensile properties of as-cast CoCrFeMnNi high entropy alloy, Materials Chemistry and Physics. 210 (2018) 136–145. https://doi.org/10.1016/j.matchemphys.2017.08.011.

[21] L. Zendejas Medina, M.V. Tavares Da Costa, E.M. Paschalidou, G. Lindwall, L. Riekehr, M. Korvela, S. Fritze, S. Kolozsvári, E.K. Gamstedt, L. Nyholm, U. Jansson, Enhancing corrosion resistance,

hardness, and crack resistance in magnetron sputtered high entropy CoCrFeMnNi coatings by adding carbon, Materials & Design. 205 (2021) 109711. https://doi.org/10.1016/j.matdes.2021.109711.

[22] Y. Zhang, Z. Zhang, Z. Jing, H. Wang, W. Yao, X. Liang, Characteristics of (Mo-Ta-W)-C and (Nb-Ta-W)-C refractory multi-principal element carbide thin films by non-reactive direct current magnetron co-sputtering, Journal of Alloys and Compounds. 936 (2023) 168260. https://doi.org/10.1016/j.jallcom.2022.168260.

[23] V. Braic, M. Balaceanu, M. Braic, A. Vladescu, S. Panseri, A. Russo, Characterization of multi-principal-element (TiZrNbHfTa)N and (TiZrNbHfTa)C coatings for biomedical applications, Journal of the Mechanical Behavior of Biomedical Materials. 10 (2012) 197–205. https://doi.org/10.1016/j.jmbbm.2012.02.020.

[24] J. Fan, X. Liu, J. Pu, Y. Shi, Anti-friction mechanism of VAlTiCrMo high-entropy alloy coatings through tribo-oxidation inducing layered oxidic surface, Tribology International. 171 (2022) 107523. https://doi.org/10.1016/j.triboint.2022.107523.

[25] G. Greczynski, D. Primetzhofer, J. Lu, L. Hultman, Core-level spectra and binding energies of transition metal nitrides by non-destructive x-ray photoelectron spectroscopy through capping layers, Applied Surface Science. 396 (2017) 347–358. https://doi.org/10.1016/j.apsusc.2016.10.152.

[26] W.C. Oliver, G.M. Pharr, An improved technique for determining hardness and elastic modulus using load and displacement sensing indentation experiments, J. Mater. Res. 7 (1992) 1564–1583. https://doi.org/10.1557/JMR.1992.1564.

[27] D.-G. Kim, T.-Y. Seong, Y.-J. Baik, Effects of annealing on the microstructures and mechanical properties of TiNyAlN nano-multilayer films prepared by ion-beam assisted deposition, Surface and Coatings Technology. (2002). https://doi.org/10.1016/S0257-8972(01)01543-2.

[28] A. Van De Walle, P. Tiwary, M. De Jong, D.L. Olmsted, M. Asta, A. Dick, D. Shin, Y. Wang, L.-Q. Chen, Z.-K. Liu, Efficient stochastic generation of special quasirandom structures, Calphad. 42 (2013) 13–18. https://doi.org/10.1016/j.calphad.2013.06.006.

[29] A. Van De Walle, Multicomponent multisublattice alloys, nonconfigurational entropy and other additions to the Alloy Theoretic Automated Toolkit, Calphad. 33 (2009) 266–278. https://doi.org/10.1016/j.calphad.2008.12.005.

[30] W. Kohn, L.J. Sham, Self-Consistent Equations Including Exchange and Correlation Effects, Phys. Rev. 140 (1965) A1133–A1138. https://doi.org/10.1103/PhysRev.140.A1133.

[31] H. Liu, H. Du, G. Xian, Y. Chen, H. Dai, Ab-initio calculations of corundum structured α-(Al0.75Cr0.22Me0.03)2O3 compounds (Me = Si, Fe, Mn, Ti, V and Y), Computational Materials Science. 212 (2022) 111601. https://doi.org/10.1016/j.commatsci.2022.111601.

[32] P.E. Blöchl, Projector augmented-wave method, Phys. Rev. B. 50 (1994) 17953–17979. https://doi.org/10.1103/PhysRevB.50.17953.

[33] J.P. Perdew, Y. Wang, Accurate and simple analytic representation of the electron-gas correlation energy, Phys. Rev. B. 45 (1992) 13244–13249. https://doi.org/10.1103/PhysRevB.45.13244.

[34] J.P. Perdew, K. Burke, M. Ernzerhof, Generalized Gradient Approximation Made Simple, Phys. Rev. Lett. 77 (1996) 3865–3868. https://doi.org/10.1103/PhysRevLett.77.3865.

[35] Z. Huang, G. Liu, B. Zhang, M. Yan, Y. Fu, A theoretical study of the stability, mechanical and thermal properties of AlNiCuCo equimolar high entropy alloy, Physics Letters A. 384 (2020) 126797. https://doi.org/10.1016/j.physleta.2020.126797.

[36] K. Momma, F. Izumi, VESTA 3 for three-dimensional visualization of crystal, volumetric and morphology data, J Appl Crystallogr. 44 (2011) 1272–1276. https://doi.org/10.1107/S0021889811038970.

[37] V. Wang, N. Xu, J.-C. Liu, G. Tang, W.-T. Geng, VASPKIT: A user-friendly interface facilitating high-throughput computing and analysis using VASP code, Computer Physics Communications. 267 (2021) 108033. https://doi.org/10.1016/j.cpc.2021.108033.

[38] J. Kang, H. Liu, H. Du, J. Shi, L. Wang, L. Yang, H. Dai, Microstructure, mechanical properties, electrical resistivity, and corrosion behavior of (AlCr)x(HfMoNbZr)1-x films, Applied Surface Science. 629 (2023) 157368. https://doi.org/10.1016/j.apsusc.2023.157368.

[39] B. Lesiak, L. Kövér, J. Tóth, J. Zemek, P. Jiricek, A. Kromka, N. Rangam, C sp2/sp3 hybridisations in carbon nanomaterials – XPS and (X)AES study, Applied Surface Science. 452 (2018) 223–231. https://doi.org/10.1016/j.apsusc.2018.04.269.

[40] Q. Zhou, J. Zhai, Resistive switching characteristics of Pt/TaO x /HfN x structure and its performance improvement, AIP Advances. 3 (2013) 032102. https://doi.org/10.1063/1.4794687.

[41] P. Guzmán, W. Aperador, L. Yate, Enhancement of the Pitting Corrosion Resistance of AISI 316LVM Steel with Ta-Hf-C/Au Bilayers for Biomedical Applications, Journal of Nanomaterials. 2017 (2017) 1–10. https://doi.org/10.1155/2017/6825250.

[42] J. Tang, X. Zhao, Y. Zuo, P. Ju, Y. Tang, Electrodeposited Pd-Ni-Mo film as a cathode material for hydrogen evolution reaction, Electrochimica Acta. 174 (2015) 1041–1049. https://doi.org/10.1016/j.electacta.2015.06.134.

[43] Y. Li, R. Zhang, L. Du, Q. Zhang, W. Wang, Catalytic mechanism of C–F bond cleavage: insights from QM/MM analysis of fluoroacetate dehalogenase, Catal. Sci. Technol. 6 (2016) 73–80. https://doi.org/10.1039/C5CY00777A.

[44] M. Deng, J. Qi, X. Li, Y. Xiao, L. Yang, X. Yu, H. Wang, B. Yuan, Q. Gao, MoC/C nanowires as high-rate and long cyclic life anode for lithium ion batteries, Electrochimica Acta. 277 (2018) 205–210. https://doi.org/10.1016/j.electacta.2018.04.185.

[45] X.Q. Jia, L. Kang, X.Y. Liu, Z.H. Wang, B.B. Jin, S.B. Mi, J. Chen, W.W. Xu, P.H. Wu, High Performance Ultra-Thin Niobium Films for Superconducting Hot-Electron Devices, IEEE Trans. Appl. Supercond. 23 (2013) 2300704–2300704. https://doi.org/10.1109/TASC.2012.2235508.

[46] C. Zhang, M. Beidaghi, M. Naguib, M.R. Lukatskaya, M.-Q. Zhao, B. Dyatkin, K.M. Cook, S.J. Kim, B. Eng, X. Xiao, D. Long, W. Qiao, B. Dunn, Y. Gogotsi, Synthesis and Charge Storage Properties of Hierarchical Niobium Pentoxide/Carbon/Niobium Carbide (MXene) Hybrid Materials, Chem. Mater. 28 (2016) 3937–3943. https://doi.org/10.1021/acs.chemmater.6b01244.

[47] J. Zhang, X. Wu, K. Yang, Q. Li, M. Guo, J. Wang, K. Pan, Z. Huang, J. He, A novel surface design for preparing a Mo-10%Nb sputtering target with ultra-low oxygen content: Coating a NbC layer on Nb powder particles via chemical vapour reaction under CH4 atmosphere, Surface and Coatings Technology. 400 (2020) 126213. https://doi.org/10.1016/j.surfcoat.2020.126213.

[48] M. El Garah, D.E. Touaibia, S. Achache, A. Michau, E. Sviridova, P.S. Postnikov, M.M. Chehimi, F. Schuster, F. Sanchette, Data on nitridation effect of AlTiTaZrHf(-N) high entropy films by X-ray photoelectron spectroscopy, Data in Brief. 42 (2022) 108241. https://doi.org/10.1016/j.dib.2022.108241.

[49] J. Wang, H. Zhang, X. Yu, L. Wang, W. Huang, Z. Lu, Insight into the structure and tribological and corrosion performance of high entropy (CrNbSiTiZr)C films: First-principles and experimental study, Surface and Coatings Technology. 421 (2021) 127468. https://doi.org/10.1016/j.surfcoat.2021.127468.

[50] Y. Chen, B. Gao, M. Wang, X. Xiao, A. Lv, S. Jiao, P.K. Chu, Dual-phase MoC-Mo2C nanosheets prepared by molten salt electrochemical conversion of CO2 as excellent electrocatalysts for the hydrogen evolution reaction, Nano Energy. 90 (2021) 106533. https://doi.org/10.1016/j.nanoen.2021.106533.

[51] S. Upadhyay, O.P. Pandey, Synthesis of Mo2C/MoC/C nanocomposite for hydrogen evolution reaction, J Solid State Electrochem. 26 (2022) 559–564. https://doi.org/10.1007/s10008-021-05096-5.

[52] K. Zhang, M. Wen, Q.N. Meng, C.Q. Hu, X. Li, C. Liu, W.T. Zheng, Effects of substrate bias voltage on the microstructure, mechanical properties and tribological behavior of reactive sputtered niobium carbide films, Surface and Coatings Technology. 212 (2012) 185–191. https://doi.org/10.1016/j.surfcoat.2012.09.046.

[53] J.-H. Ryu, C. Mahata, S. Kim, Long-term and short-term plasticity of Ta2O5/HfO2 memristor for hardware neuromorphic application, Journal of Alloys and Compounds. 850 (2021) 156675. https://doi.org/10.1016/j.jallcom.2020.156675.

[54] H. Hamad, E. Bailón-García, A.F. Pérez-Cadenas, F.J. Maldonado-Hódar, F. Carrasco-Marín, ZrO2-TiO2/Carbon core-shell composites as highly efficient solar-driven photo-catalysts: An approach for removal of hazardous water pollutants, Journal of Environmental Chemical Engineering. 8 (2020) 104350. https://doi.org/10.1016/j.jece.2020.104350.

[55] A. Leyland, A. Matthews, On the significance of the H/E ratio in wear control: a nanocomposite coating approach to optimised tribological behaviour, Wear. 246 (2000) 1–11. https://doi.org/10.1016/S0043-1648(00)00488-9.

[56] H. Du, L. Wang, M. Young, H. Zhao, J. Xiong, W. Wan, Structure and properties of lanthanum doped AlCrN coatings, Surface and Coatings Technology. 337 (2018) 439–446. https://doi.org/10.1016/j.surfcoat.2018.01.060.

[57] L. Haus, M. Wildfeuer, J.-E. Grochowski, J. Wöckel, M. Müller, F. Köhn, W. Schulz, C. Wüstefeld, D. Rafaja, J. Albrecht, Wear properties of carbon-rich tungsten carbide films, Wear. 488–489 (2022) 204146. https://doi.org/10.1016/j.wear.2021.204146.

[58] H. Li, L. Zhang, Q. Zeng, K. Guan, K. Li, H. Ren, S. Liu, L. Cheng, Structural, elastic and electronic properties of transition metal carbides TMC (TM=Ti, Zr, Hf and Ta) from first-principles calculations, Solid State Communications. 151 (2011) 602–606. https://doi.org/10.1016/j.ssc.2011.02.005.

[59] Y. Yang, H. Lu, C. Yu, J.M. Chen, First-principles calculations of mechanical properties of TiC and TiN, Journal of Alloys and Compounds. 485 (2009) 542–547. https://doi.org/10.1016/j.jallcom.2009.06.023.

[60] S. Jiang, L. Shao, T.-W. Fan, J.-M. Duan, X.-T. Chen, B.-Y. Tang, Elastic and thermodynamic properties of high entropy carbide (HfTaZrTi)C and (HfTaZrNb)C from ab initio investigation, Ceramics International. 46 (2020) 15104–15112. https://doi.org/10.1016/j.ceramint.2020.03.045.

[61] C. Sun, Y. Zheng, L. Chen, F. Fang, X. Zhou, J. Jiang, Thermodynamic stability and mechanical properties of (V, M)C (M = W, Mo and Cr) multicomponent carbides: A combined theoretical and experimental study, Journal of Alloys and Compounds. 895 (2022) 162649. https://doi.org/10.1016/j.jallcom.2021.162649.

[62] H. Lasfargues, T. Glechner, C.M. Koller, V. Paneta, D. Primetzhofer, S. Kolozsvári, D. Holec, H. Riedl, P.H. Mayrhofer, Non-reactively sputtered ultra-high temperature Hf-C and Ta-C coatings, Surface and Coatings Technology. 309 (2017) 436–444. https://doi.org/10.1016/j.surfcoat.2016.11.073.

[63] K. Zhang, M. Wen, G. Cheng, X. Li, Q.N. Meng, J.S. Lian, W.T. Zheng, Reactive magnetron sputtering deposition and characterization of niobium carbide films, Vacuum. 99 (2014) 233–241. https://doi.org/10.1016/j.vacuum.2013.06.012.

[64] H.W. Hugosson, O. Eriksson, U. Jansson, B. Johansson, Phase stabilities and homogeneity ranges in 4 d -transition-metal carbides: A theoretical study, Phys. Rev. B. 63 (2001) 134108. https://doi.org/10.1103/PhysRevB.63.134108.

[65] P. Sarker, T. Harrington, C. Toher, C. Oses, M. Samiee, J.-P. Maria, D.W. Brenner, K.S. Vecchio, S. Curtarolo, High-entropy high-hardness metal carbides discovered by entropy descriptors, Nat Commun. 9 (2018) 4980. https://doi.org/10.1038/s41467-018-07160-7.

[66] T. Yang, L. Ni, Q. Zheng, J. Xiong, Cutting wear, microstructure and mechanical properties of (Ti 0.5 ,W 0.5)C-based cermet inserts containing Mo 2 C, International Journal of Refractory Metals and Hard Materials. 68 (2017) 151–158. https://doi.org/10.1016/j.ijrmhm.2017.07.011.

[67] S.A. Ghaffari, M.A. Faghihi-Sani, F. Golestani-Fard, M. Nojabayy, Diffusion and solid solution formation between the binary carbides of TaC, HfC and ZrC, International Journal of Refractory Metals and Hard Materials. 41 (2013) 180–184. https://doi.org/10.1016/j.ijrmhm.2013.03.009.

[68] H.O. Pierson, Handbook of Refractory Carbides and Nitrides: Properties, Characteristics, Processing and Applications, Elsevier Science, 1996.

[69] S. Kavak, K.G. Bayrak, M. Bellek, S. Mertdinç, F. Muhaffel, H. Gökçe, E. Ayas, B. Derin, M.L. Öveçoğlu, D. Ağaoğulları, Synthesis and characterization of (HfMoTiWZr)C high entropy carbide ceramics, Ceramics International. 48 (2022) 7695–7705. https://doi.org/10.1016/j.ceramint.2021.11.317.

[70] U. Jansson, E. Lewin, Sputter deposition of transition-metal carbide films — A critical review from a chemical perspective, Thin Solid Films. 536 (2013) 1–24. https://doi.org/10.1016/j.tsf.2013.02.019.

[71] T.J. Harrington, J. Gild, P. Sarker, C. Toher, C.M. Rost, O.F. Dippo, C. McElfresh, K. Kaufmann, E. Marin, L. Borowski, P.E. Hopkins, J. Luo, S. Curtarolo, D.W. Brenner, K.S. Vecchio, Phase stability and mechanical properties of novel high entropy transition metal carbides, Acta Materialia. 166 (2019) 271–280. https://doi.org/10.1016/j.actamat.2018.12.054.

[72] A. Takeuchi, A. Inoue, Classification of Bulk Metallic Glasses by Atomic Size Difference, Heat of Mixing and Period of Constituent Elements and Its Application to Characterization of the Main Alloying Element, Mater. Trans. 46 (2005) 2817–2829. https://doi.org/10.2320/matertrans.46.2817.

[73] G. Greczynski, L. Hultman, Towards reliable X-ray photoelectron spectroscopy: Sputter-damage effects in transition metal borides, carbides, nitrides, and oxides, Applied Surface Science. 542 (2021) 148599. https://doi.org/10.1016/j.apsusc.2020.148599.

[74] Y. Yu, G. Kim, B. Jeong, J.-I. Park, H.-J. Shin, K.-S. Park, J. Lee, K. Kim, In situ photoelectron spectroscopy for characterizing the chemical evolution of a carbon steel surface by heat-treatment, Applied Surface Science. 608 (2023) 155155. https://doi.org/10.1016/j.apsusc.2022.155155.

[75] J. Li, R. Ge, P. Lan, J. Yang, J. Feng, Y. Li, S. Li, B. Liu, W. Li, In situ phase transition induced TM–MoC/Mo2C (TM= Fe, Co, Ni, and Cu) heterostructure catalysts for efficient hydrogen evolution, J. Mater. Chem. A. 10 (2022) 10493–10502. https://doi.org/10.1039/D2TA00727D.

[76] J. Liu, X. Li, X. Liang, H. Fu, M. Rettenmayr, D. Liu, Structure and properties of niobium carbide coated vanadium composite membranes for high temperature hydrogen separation, Journal of Alloys and Compounds. 900 (2022) 163530. https://doi.org/10.1016/j.jallcom.2021.163530.

[77] J. Dusza, P. Švec, V. Girman, R. Sedlák, E.G. Castle, T. Csanádi, A. Kovalčíková, M.J. Reece, Microstructure of (Hf-Ta-Zr-Nb)C high-entropy carbide at micro and nano/atomic level, Journal of the European Ceramic Society. 38 (2018) 4303 – 4307. https://doi.org/10.1016/j.jeurceramsoc.2018.05.006.

[78] C.-H. Lai, M.-H. Tsai, S.-J. Lin, J.-W. Yeh, Influence of substrate temperature on structure and mechanical, properties of multi-element (AlCrTaTiZr)N coatings, Surface and Coatings Technology. 201 (2007) 6993–6998. https://doi.org/10.1016/j.surfcoat.2007.01.001.

[79] P. Edalati, A. Mohammadi, M. Ketabchi, K. Edalati, Microstructure and microhardness of dual-phase high-entropy alloy by high-pressure torsion: Twins and stacking faults in FCC and dislocations in BCC, Journal of Alloys and Compounds. 894 (2022) 162413. https://doi.org/10.1016/j.jallcom.2021.162413.

[80] Q. Fang, Y. Chen, J. Li, C. Jiang, B. Liu, Y. Liu, P.K. Liaw, Probing the phase transformation and dislocation evolution in dual-phase high-entropy alloys, International Journal of Plasticity. 114 (2019) 161–173. https://doi.org/10.1016/j.ijplas.2018.10.014.

[81] X. Li, D.L. Irving, L. Vitos, First-principles investigation of the micromechanical properties of fcc-hcp polymorphic high-entropy alloys, Sci Rep. 8 (2018) 11196. https://doi.org/10.1038/s41598-018-29588-z.

[82] X. Chang, M. Zeng, K. Liu, L. Fu, Phase Engineering of High-Entropy Alloys, Adv. Mater. 32 (2020) 1907226. https://doi.org/10.1002/adma.201907226.

[83] S. Wu, D. Qiao, H. Zhao, J. Wang, Y. Lu, A novel NbTaW0.5 (Mo2C)x refractory high-entropy alloy with excellent mechanical properties, Journal of Alloys and Compounds. 889 (2021) 161800. https://doi.org/10.1016/j.jallcom.2021.161800.

[84] H. Larhlimi, A. Ghailane, M. Makha, J. Alami, Magnetron sputtered titanium carbide-based coatings: A review of science and technology, Vacuum. 197 (2022) 110853. https://doi.org/10.1016/j.vacuum.2021.110853.

[85] P. Eklund, M. Beckers, U. Jansson, H. Högberg, L. Hultman, The M+1AX phases: Materials science and thin-film processing, Thin Solid Films. 518 (2010) 1851–1878. https://doi.org/10.1016/j.tsf.2009.07.184.

[86] E. Rabinowicz, A. Mutis, Effect of abrasive particle size on wear, Wear. 8 (1965) 381–390. https://doi.org/10.1016/0043-1648(65)90169-9.

List of figure captions

Fig. 1 (a) Elemental compositions and (b) the atomic ratio of carbon and the total metallic elements *C/Me* of (HfMoNbZr)C_x films as a function of graphite target power P_C.

Fig. 2 (a) X-ray diffractograms, (b) out-of-plane lattice constant a_0, and (c) full width at half maximum FWHM of the (HfMoNbZr)C_x films grown at different graphite target power P_C. Both a_0 and FWHM are estimated from positions of FCC 111 peak for P_C of 45, 60, 80,100, and 120 W, and BCC 110 peak for P_C = 0 W.

Fig. 3 The cross-sectional morphology of (HfMoNbZr)C_x films deposited at different P_C: (a) 0W, (b) 45 W, (c) 60 W, (d) 80 W, (e) 100 W, (f) 120 W.

Fig. 4 High-resolution core level spectra of (a) C 1s, (b) Hf 4f, (c) Mo 3d, (d) Nb 3d, (e) Zr 3d, and (f) O 1s recorded from (HfMoNbZr)C_x films.

Fig. 5 (a) The hardness H and elastic modulus E, and (b) H/E and H^3/E^{*2} of (HfMoNbZr)C_x films as a function of graphite target power P_C. H and E are averaged from 10 indentations.

Fig. 6 (a) The coefficient of friction (COF) as a function of sliding time, (b) average COF, (c) 2D profiles of wear tracks, and (d) wear rate, of the (HfMoNbZr)C_x films deposited at different P_C. The average COF is averaged from 3 measurements. The wear rate is averaged from 6 measurements.

Fig. 7 (a) Total density of state (TDOS) and partial density of states (PDOS) of (b) C, (c) Hf, (d) Mo, (e) Nb, and (f) Zr for ($Hf_{0.25}Mo_{0.25}Nb_{0.25}Zr_{0.25}$)C. The Fermi level is set to 0 eV and marked by black dashed line.

Fig. 1

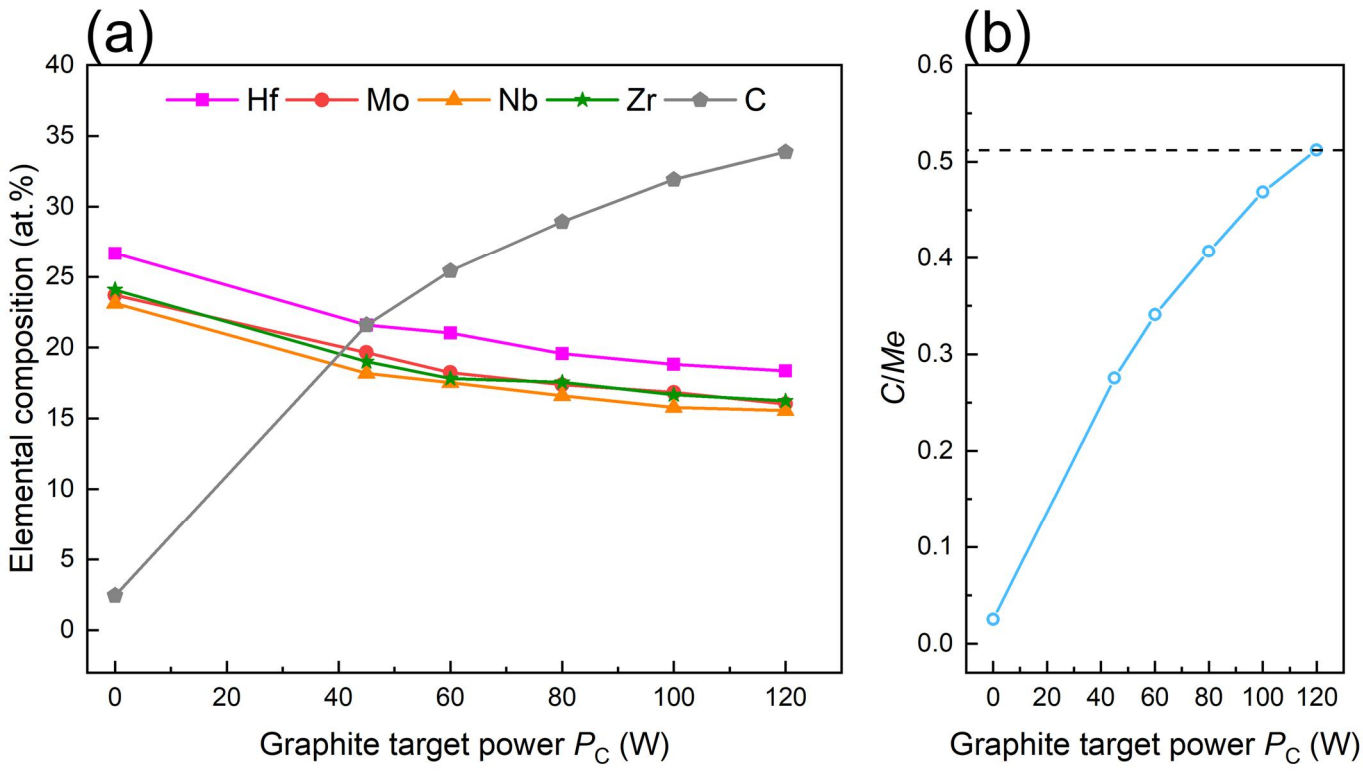
(a)
Hf
Mo
Nb
Zr
C
Elemental composition (at.%)
Graphite target power P_C (W)
(b)
C/Me
Graphite target power P_C (W)

Fig. 2

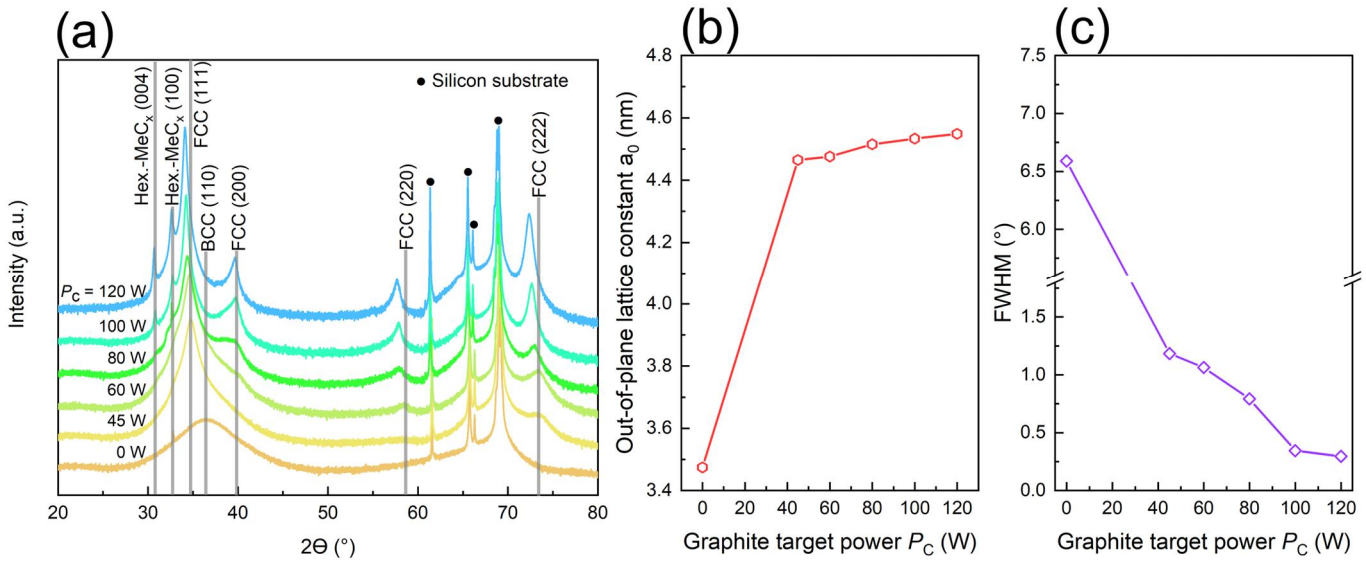
(a)
Intensity (a.u.)
2Θ (°)
Hex.-MeCx (004)
Hex.-MeCx (100)
FCC (111)
BCC (110)
FCC (200)
FCC (220)
FCC (222)
● Silicon substrate
PC = 120 W
100 W
80 W
60 W
45 W
0 W
(b)
Out-of-plane lattice constant a0 (nm)
Graphite target power PC (W)
(c)
FWHM (°)
Graphite target power PC (W)

Fig. 3

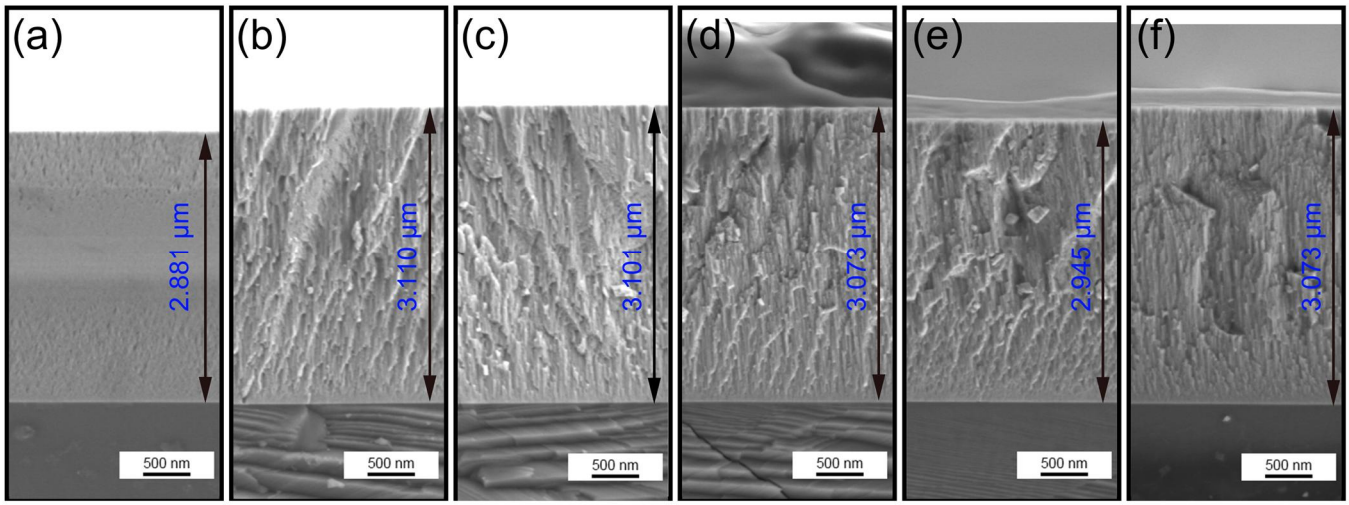
(a)
2.881 µm
500 nm
(b)
3.110 µm
500 nm
(c)
3.101 µm
500 nm
(d)
3.073 µm
500 nm
(e)
2.945 µm
500 nm
(f)
3.073 µm
500 nm

Fig. 4

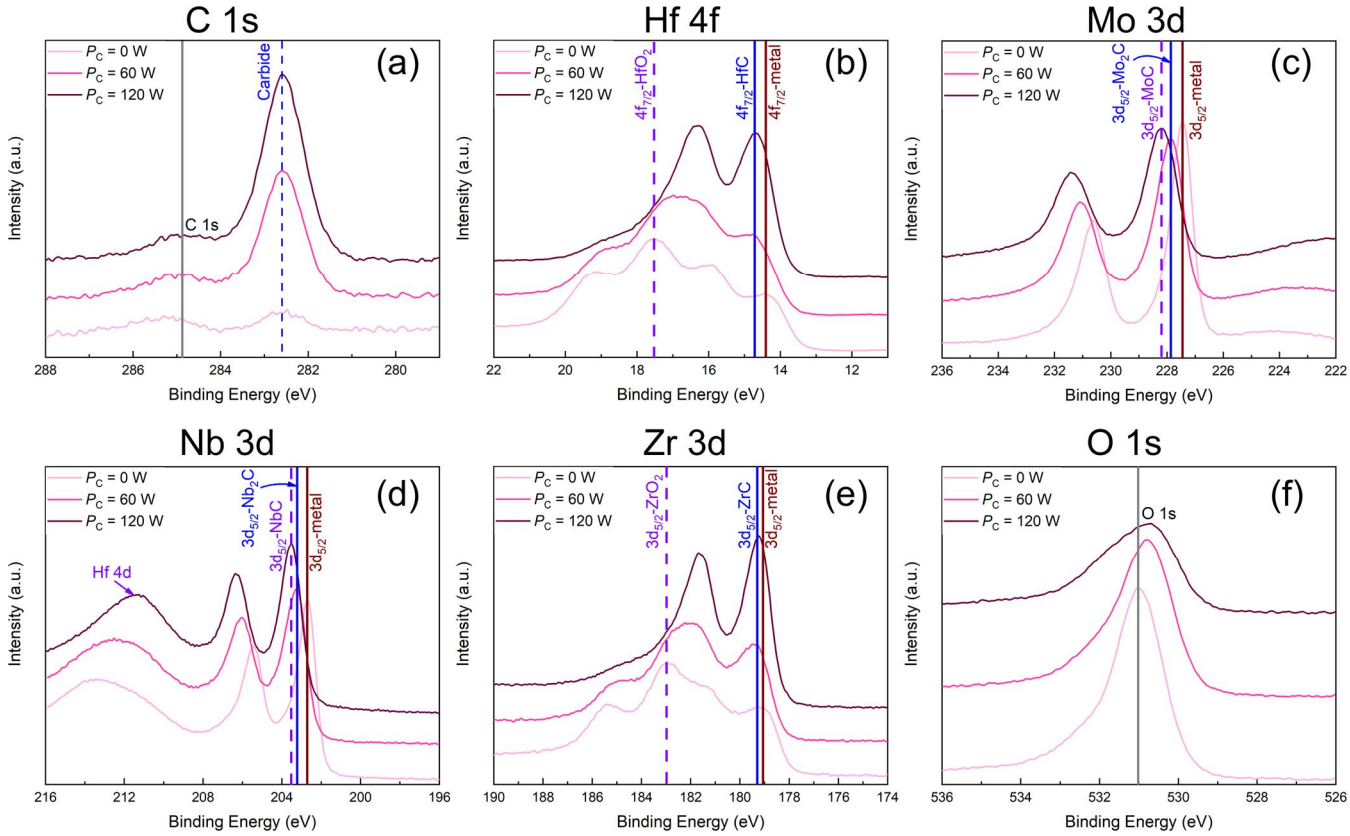
C 1s
(a)
P_C = 0 W
P_C = 60 W
P_C = 120 W
Carbide
C 1s
Intensity (a.u.)
Binding Energy (eV)
Hf 4f
(b)
$4f_{7/2}$-HfO_2
$4f_{7/2}$-HfC
$4f_{7/2}$-metal
Mo 3d
(c)
$3d_{5/2}$-Mo_2C
$3d_{5/2}$-MoC
$3d_{5/2}$-metal
Nb 3d
(d)
Hf 4d
$3d_{5/2}$-Nb_2C
$3d_{5/2}$-NbC
$3d_{5/2}$-metal
Zr 3d
(e)
$3d_{5/2}$-ZrO_2
$3d_{5/2}$-ZrC
$3d_{5/2}$-metal
O 1s
(f)
O 1s

Fig. 5

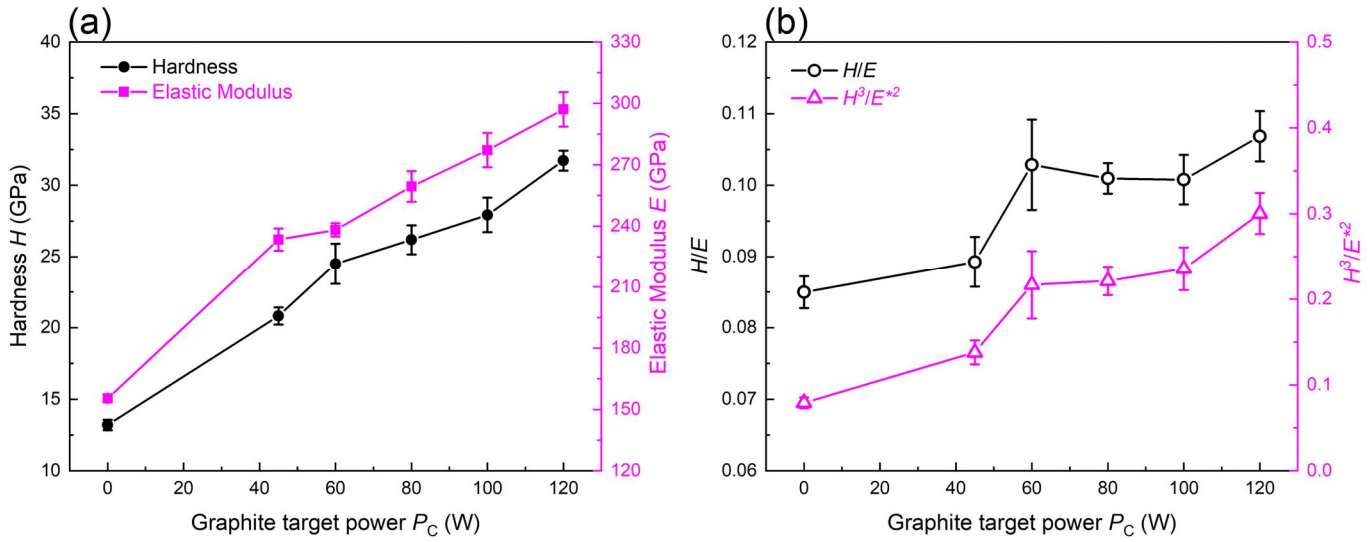
(a)
Hardness
Elastic Modulus
Hardness H (GPa)
Elastic Modulus E (GPa)
Graphite target power P_C (W)
(b)
H/E
H^3/E^{*2}
H/E
H^3/E^{*2}
Graphite target power P_C (W)

Fig. 6

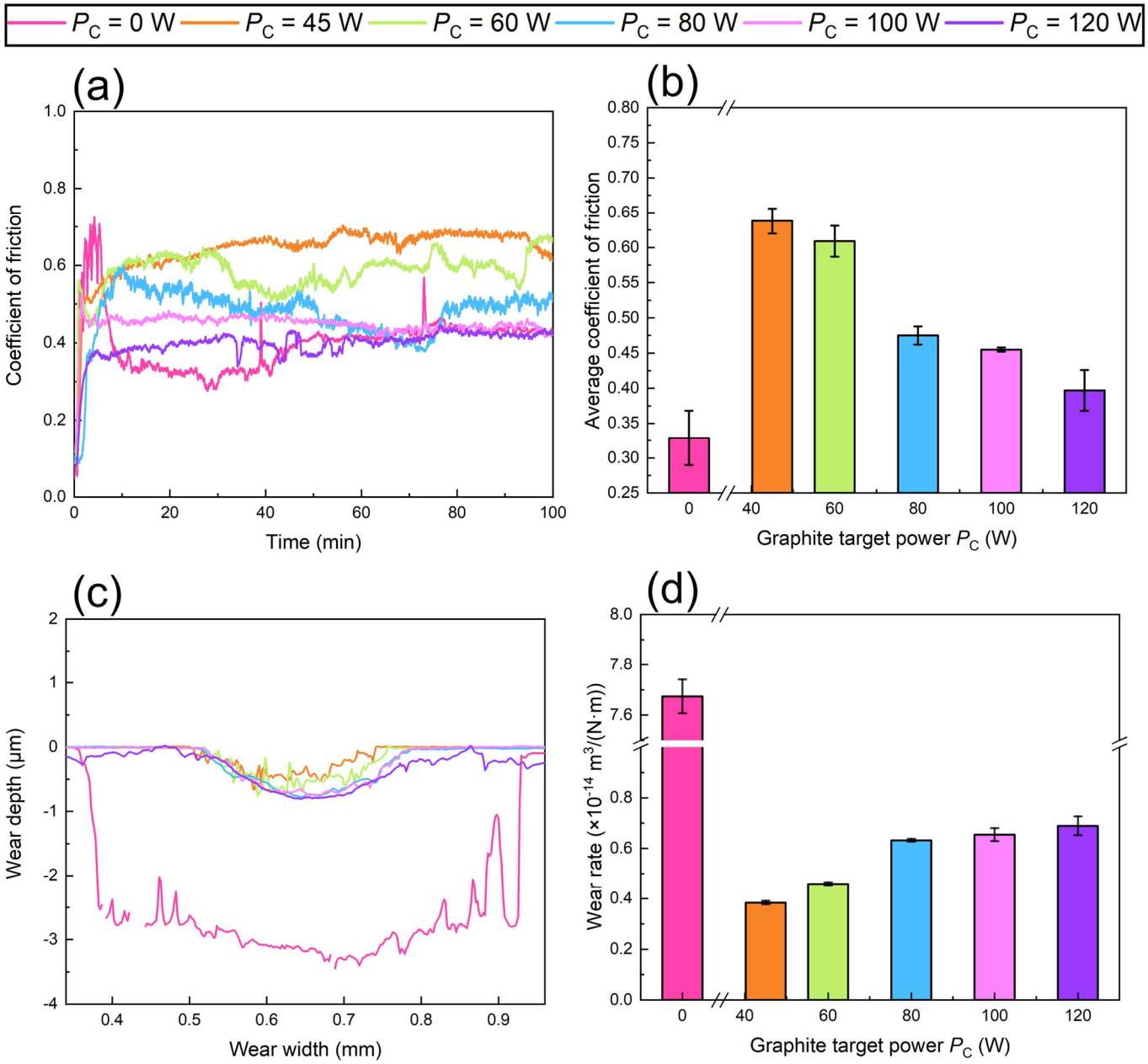
P_C = 0 W
P_C = 45 W
P_C = 60 W
P_C = 80 W
P_C = 100 W
P_C = 120 W
(a)
Coefficient of friction
Time (min)
(b)
Average coefficient of friction
Graphite target power P_C (W)
(c)
Wear depth (μm)
Wear width (mm)
(d)
Wear rate (×10^{-14} m^3/(N·m))
Graphite target power P_C (W)

Fig. 7

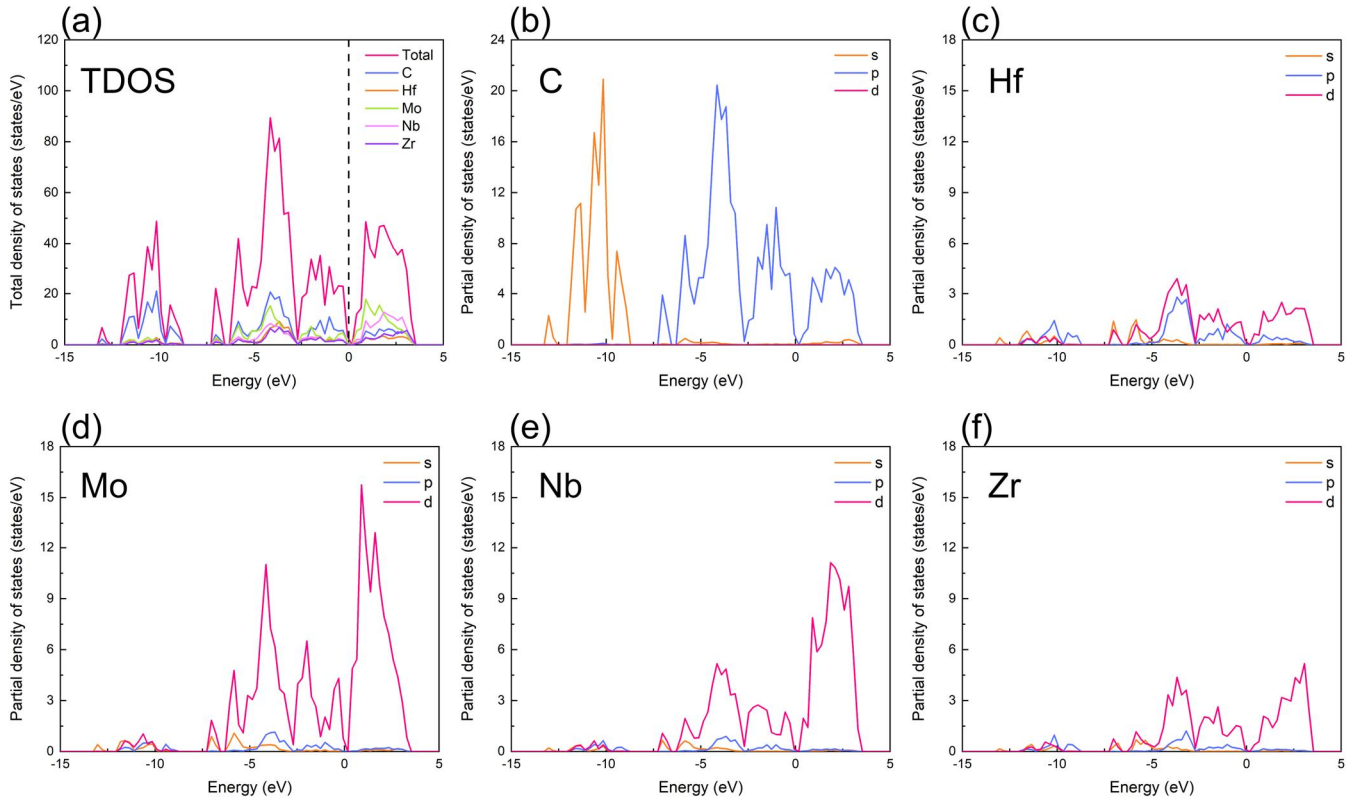
(a)
TDOS
Total
C
Hf
Mo
Nb
Zr
Total density of states (states/eV)
Energy (eV)
(b)
C
s
p
d
Partial density of states (states/eV)
Energy (eV)
(c)
Hf
s
p
d
Partial density of states (states/eV)
Energy (eV)
(d)
Mo
s
p
d
Partial density of states (states/eV)
Energy (eV)
(e)
Nb
s
p
d
Partial density of states (states/eV)
Energy (eV)
(f)
Zr
s
p
d
Partial density of states (states/eV)
Energy (eV)